

¹ Masters Thesis: The Evolution of Fault Slip Surfaces with
² Cumulative Displacement

³ Kelian Dascher-Cousineau

⁴ February 28, 2017

⁵ **Abstract**

Fault slip surface roughness determines fault strength, friction and dynamic fault processes. Wear models and field observations suggest that roughness decreases with cumulative displacement. However, measurements have yet to isolate the effect of displacement from other possible controls, such as lithology or tectonic setting. We present an unprecedentedly large fault surface dataset collected in and around the San-Rafael Desert, S.E. Utah, United States. In the study area, faults accommodated regional extension at shallow 1 to 3 km depth and are hosted in the massive, well sorted, high porosity Navajo and Entrada sandstones. Existing detailed stratigraphic throw profile provide a maximum constraint for displacement. Where cross-sectional exposure is good, we measure exact displacement imparted on slip surfaces using offset in marker horizons. Thereby, we isolate for the effect of displacement during the embryonic stages of faulting (0 to 60 m in displacement). Our field observations indicate a clear compositional and morphological progression from isolated joints or deformation bands towards smooth, continuous and mirror-like fault slip surfaces with increasing displacement. To quantify these observations, slip surfaces were scanned with a white light interferometer, a laser scanner and a ground based Lidar. Together these instruments resolve more than eight decades of spatial bandwidth (from less than μm 's to m's in scale). Preliminary results indicate that roughness decreases with displacement according to a power law. Roughness measurement associated with only maximum constraints on displacements corroborate this result—for a given displacement, minimum roughness is bounded by the later smoothing trend. In addition, we find that the maximum roughness is fixed—bounded a by a primordial roughness corresponding to that of joints surfaces and deformation band edges. Our results build towards a coherent model of fault wear robust to ambiguities associated to displacement estimates, spatial scaling and geological context.

³⁰ *Will have to include relationship to white light data, modelling results/interp*

³¹ **Contribution of Authors**

³² **1 Introduction**

Faults are a characteristic feature of the Earth's brittle crust. Fluid flow, seismicity and crustal mineralization are just few systems upon which faults act as major controls (Sibson, 1977). In spite of their importance, some aspects of faults and their underlying processes remain poorly understood. How strong is a fault? How do faults mature? Are small faults mechanically different to large faults? Fault geometry has been shown to be a key parameter controlling the mechanical behavior and evolution of faults (e.g. Lay et al., 1982; Aki, 1984; Power et al. 1988; Chester and Chester, 2000), but these questions are not yet fully answered.

Slip on a fault occurs on discrete slip surfaces in fault zones (Davatzes and Aydin, 2005). These surfaces are not planar; they are rough. Roughness is observable at all scales (Scholtz and Aviles, 1986; Candela et al., 2012). Slickenlines, corrugations, mullions and jogs are all surface features that can be seen at different length scales (Sagy and Brodsky, 2009). Field studies have found common characteristics in the topography of fault surfaces. These can be summarized as follows: 1) Fault surfaces appear to be well defined by large fractal domains, wherein 2) faults are smoother at larger length scales (Scholtz and Aviles, 1986; Candela et al., 2012), 3) rougher in the slip perpendicular direction than in the slip parallel direction (Lee and Bruhn, 1996), and 4) slip surfaces are smoother with cumulative displacement (Sagy et al., 2007). Fault roughness has been demonstrated to be critical in determining the strength (Chester and Chester, 2000, Brodsky et al., 2016), triggering (Parsons, 2008), dynamic properties (Candela et al., 2011; Dunham et al., 2011), spatial distribution (Parson, 2008) and failure recurrence of faults (Stirling et al., 1996). It is increasingly evident that roughness is a fingerprint of fundamental features of the faulting process (Brodsky et al., 2016). In accordance, incorporating more complex sources geometries has become a more frequent practice in dynamic earthquake rupture modelling (Shi and Day, 2013; Dunham et al., 2011).

Changes in roughness, as determined by cumulative displacement (Sagy et al, 2007; Brodsky et al, 2011), imply faults mature. Fundamental differences between immature and mature fault have far-reaching implications. Fixed source parameter scaling of earthquakes is a pillar of earthquake seismology. However, analysis of seismic signals of immature faults vs. mature faults suggest that scaling is sensitive to cumulative displacement. This observation leads to an interpretation of fundamental differences in earthquake populations. Specifically fault maturation would undermine the applicability of a constant magnitude scaling. Evolving mechanical properties such as fault friction and static strength—both associated to fault roughness—would imply that immature and mature faults belong to distinct populations with distinct scaling. (Harrington and Brodsky, 2011)

While there has been significant progress in understanding the role of roughness in the faulting process, how and why fault surfaces change is still unclear (e.g. Candela et al., 2011; Dunham et al., 2011; Brodsky et al., 2016). Sagy et al. (2007) noted a systematic decrease in roughness of ‘mature’, large displacement faults compared to ‘immature’ faults with low displacements. Similar results have since been observed along reactivated joints, in laboratory experiments (Davidesko et al., 2014), and in compilations of fault roughness analysis (Brodsky et al., 2011; Candela et al., 2012). These studies all attribute the decrease in roughness to wear at the fault interface. However, these data show only weak correlations between fault roughness and cumulative displacement. Indeed, relating roughness and cumulative displacement is not trivial. Fault surfaces in exhumed faults are rarely well preserved. Furthermore, obtaining well-constrained displacement estimates is contingent on the presence of precise and accurate kinematic indicators. Combining observations over a broad range of displacements is challenging. Consequently, it is unclear whether trends observed in compilations of roughness measurements from multiple faults are directly attributable to displacement or a combination other geological factors. For instance, while comparing fault surfaces from geologically diverse datasets, variations in lithology, faulting mechanism, temperature and depth may all be introducing further systematic variations.

Additionally, the evolution of roughness represents a novel insight into the architecture of a fault zone. The geometry of the fault surface modulates the architecture of the whole fault zone (Mitchell and Faulkner, 2009). Changes in roughness require interaction between the slip surfaces and its direct surrounding (fault core), resulting in the formation of fault rock (Power and Tullis, 1988). In addition to earthquake mechanics, the architecture of a fault zone, and its corresponding permeability structure, is very important for hydrocarbon exploration (Shipton and Cowie, 2003). However, because the change in roughness by wear is poorly understood,

90 the equivalent production of wear material, the fault rock, is also poorly understood. Fault
91 rock thickness growth with displacement is documented (Sholtz, 1987), but variability is such
92 that even order of magnitude estimates of thickness for a given displacement are unavailable.

93 In this study, we report on how fault surfaces change. In line with previous studies, I hy-
94 pothesize that faults smooth with displacement and that wear is a dominant mechanism in the
95 evolution of fault surfaces with cumulative displacement. We measure the surface roughness
96 of natural fault surfaces with varying displacements to confirm and better quantify the role of
97 cumulative displacement on fault roughness. Field work in Southern Utah was conducted to
98 collect scans of pristine fault surfaces with terrestrial laser scanners and hand-samples for labo-
99 ratory high resolution scans. Fault roughness is then be quantified and related to corresponding
100 displacement. A robust quantitative correlation between roughness and cumulative displace-
101 ment enables the parameterization of semi-analytical wear model for fault surfaces. Moreover,
102 based on my results, I produce an external estimate of fault rock production in the fault zone.

103 1.1 Fault Roughness

104 The deviation from planarity formally defines roughness (Brown and Scholz, 1985). Pioneering
105 studies used contact profilometers to measure the roughness of fault surfaces (Scholz and Aviles,
106 1986; Power and Tullis, 1991. Combined with surface profiles of large scale continental faults,
107 faults were found to have a remarkably broad fractal band ranging over 10 orders of magni-
108 tude—from 10^{-5} to $10^5 m$ (Scholz and Aviles, 1986). Over these length scales, fractal scaling is
109 said to be statistically self-affine. A statistically self-affine profile along x with heights $h(x)$, is
110 invariant under the affine transformation:

$$\left\{ \begin{array}{l} x \rightarrow \lambda x \\ h \rightarrow \mu h \end{array} \right\} \quad (1)$$

111 This relation therefore implies an exponential relation between the scaling, λ (along x), and
112 μ (along h) such that:

$$\mu = \lambda^\varsigma \quad (2)$$

113 Where ς is a constant named the Hurst exponent. Note that self-similarity, is an instance
114 of self-affinity where the Hurst exponent is 1 (Schmittbulh et al., 1993). Developments in laser
115 scanner technology over the past decade, particularly terrestrial laser scanners, allowed surfaces
116 to be characterized by calculating the Hurst exponent from thousands of cross sectional profiles
117 through a fault surface (e.g. Candela et al., 2012). Studies of natural mode I crack surfaces have
118 observed self-affinity with a Hurst exponent of ~ 0.8 at all scales of observation (Scholtz, 1985).
119 Shear, or mode II cracks (i.e. faults) are different. They are anisotropic—the Hurst exponent
120 parallel to shear (~ 0.6) is smaller than that in the shear-perpendicular direction (~ 0.8) (Lee
121 and Bruhn, 1996).

122 Another parameter is required to fully describe surface roughness. While the Hurst ex-
123 ponent describes the scaling behavior of the roughness it does not define the magnitude of
124 the roughness. The pre-factor defines the amplitude of the scaling law (Candela et al., 2009).
125 The pre-factor is subject to significant variation. Overall, observations show that fault surfaces
126 have distinctly smoother profiles along slip direction than perpendicular to slip (Lee and Bruhn,
127 1996). Many methods exist to quantify roughness scaling, possibly most intuitive of which is
128 the Root Mean Squared (RMS) as a function of scale. For a profile of length L with a point
129 spacing of Δx with deviation h from the best fit line, the RMS for a given scale s is defined as
130 follows:

$$RMS(s) = \sqrt{\frac{\Delta x}{L} \sum_{i=1}^{L/\Delta x} h_i^2} \quad (3)$$

The *RMS* roughness of a fault or fracture exhibits power-law scaling with segment length. A self-affine profile should therefore plot as a straight line on a log-log plot of the *RMS* as a function of the segment length with a slope equivalent to the Hurst exponent. (Schmittbuhl et al., 1993) The power spectrum of a surface profile has been shown to yield more robust roughness metrics (Schmittbuhl et al., 1993; Candela et al., 2009). For a set of discretely sampled points, the power spectrum of a profiles is the result of a Fast Fourier Transform (FFT). The spectrum defines the surface profile as superposition of sinusoidal profiles. In the frequency domain, rougher profiles will have correspondingly higher amplitudes, or power. The power spectrum, $P(k)$, of a self-affine profile (again in log-log space) defines a line as follows:

$$P(k) = Ck^{(-1-2\zeta)} \quad (4)$$

Where k is the frequency and C is the pre-factor (Candela et al., 2009).

1.2 Wear

1.3 The evolution of slip surfaces with displacement

talk about deformation in sandstones, e.g. aydin, fossen etc.

In this project, I hope to address how slip surfaces change. Many processes could cause the slip surface to change. In fact, the cause of change to the slip surface is not uniquely recorded by the roughness. Fundamentally, a fault surface can only change according to the following mechanisms:

Addition of material

Redefinition of the slip surface by fracture

Removal of material

I have hypothesized that the change in surface roughness is the result of wear—an instance of removal of material. As fault blocks slide past each other, frictional wear is an inevitable process. Layers of comminuted fault rock are direct evidence of this process (Power and Tuillis 1988). Wear is the subject of a vast field of research, particularly in engineering and tribology due to interest in lubricating and manufacturing machine parts for longevity (Meng and Ludema, 1995). Here, I outline only basic wear mechanics (i.e. Archard, 1953). Wear is formally defined as frictionally induced volume removal from surfaces in sliding contact. The wear rate, the amount of wear per unit distance is broadly related to the real area of contact and loading. When two surfaces are put in direct contact, the real area of contact is much smaller than the nominal surface areas because the load is supported at microscopic protrusions from a surface, called asperities. Remote loading normal to the surface causes local stresses and associated deformations at contact points. Note that as the load is increased, deformation of large asperities causes new asperities to come in contact. In its simplest form, wear rate defined as:

$$W \propto \frac{P}{a} \quad (5)$$

Where W is the wear rate, P is the remote load and a is a mean measure of the dimensions of the asperities in contact during sliding. The relation has been shown to be reasonably robust

in experimentation for most materials. In further detail, the size, distribution and duration of contact areas, as well as the shape of the worn particles, control the general behavior of wear. Note that material properties are implicitly buried in a probability factor—the probability of a collision of asperities to lead to removal of material (Archard, 1953). If and how wear affect the geometry of a fault slip surface remains unclear. Both field and laboratory experiment show that wear is scale dependent, such that asperities are worn down at different rates according to their typical dimensions. Asperities at longer characteristic wavelengths and larger amplitudes wear down faster, on average, than those with small wave lengths and small amplitudes. These observations correspond to both a downward translation and clockwise rotation of the self-affine scaling in the power spectrum. The exact mechanism causing this behavior is unclear. Davidesko et al., 2014 suggest that dilation during displacement on a fault ‘shelters’ smaller, shorter wavelength, asperities and therefore wears down large, long wavelength asperities. In this study, I hope to be able to relate changes in the slip surface geometry to wear processes. Specifically, empirically identifying and determining the rate of wear as expressed in the slip surface would be of particular interest. A potential caveat to the simple wear models (i.e. Archard, 1953) is the sensitivity of fault rock to sliding velocity and the presence of lubricant (e.g. pseudotachylyte, amorphous silica gel and gouge). Moreover, the stresses imparted by a propagating fault rupture front are mechanically distinct from those related to rubbing surfaces. Such a distinction may also drastically alter the relation between wear material and the slip surface (Sibson, 1977). Since Archard (1953), models of wear tend to diverge in their results, assumptions and by association, their applicability (Meng and Ludema, 1995). For the purpose of this study, the fractal nature of fault surfaces is important to reconcile with a model of wear. What is the scaling behavior of wear? Fractal surfaces are difficult to integrate into the pre-existing framework of wear processes. Specifically, defining the real area of contact, corresponding deformation and, by association, the scale dependence of wear is non-trivial (e.g. Persson, 2001; Jackson and Streator, 2006).

2 Geology

All data presented in this study was collected in the San-Rafael Desert, Utah (see figure 1). The San Rafael Desert hosts a sequence of gently dipping marine and sub-areal sedimentary rocks deposited from the Pennsylvanian to the Jurassic (see Figure 2). The San Rafael Desert is part of the San Rafael Swell, a monocline that formed when these sediments were uplifted as a passive drape fold above a reactivated basement reverse fault during the Late Cretaceous Laramide Orogeny (Kelly, 1955; Vrolijk et al., 2005). The swell is part of the broader Colorado Plateau (Kelly, 1955). Networks of joints and normal faults associated to further Laramide activity cross-cut sedimentary sequence accommodating North-South extension (Aydin and Johnson, 1978; Vrolijk et al., 2005). Within the San Rafael Swell we focus the following field locations: 1) the Chimney Rock Fault Array, 2) the Big Hole fault and 3) a network of deformation bands in the Entrada formation near Goblin Valley State Park. Advantages of theses field locations are manifold. First, the nearly pure quartzite lithology, extensional tectonic regime, depth (2-4 km or 40-80 MPa), temperature (estimates range from 45-90 °C) of activity, and faulting mechanism are all relatively consistent (Vrolijk et al., 2005). Consistency in these parameters is key to isolating the effect of displacement on the fault roughness. Moreover, both field locations exhibit well preserved fault surfaces that are exposed and accessible (see Figure 3). The Chimney Rock fault array is an orthorhombic set of faults that crops out at the northern end of the San Rafael Swell (Krantz, 1989, Davatzes et al., 2003). Two pairs of oppositely dipping normal faults crop out at the surface with preserved fault scarps. WNW-striking faults are interpreted to have formed by shear reactivation of joints, whereas ENE-striking faults initially formed from deformation bands (Davatzes, 2003). Exposure is very good, faults are abundant and have

well preserved fault surfaces (Vrolijk et al., 2005). The Chimney fault array has studied to better understand of fault geometry (Shipton and Cowie, 2001; Shipton and Cowie, 2003), permeability (Shipton et al., 2002) and kinematics (Krantz, 1986; Krantz, 1989; Maerten et al., 2001; Davatzes et al., 2003) . As a result, detailed maps of the fault array have been produced (e.g. Maerten et al., 2001) . In addition, by using measurements of the separation between footwall and hanging wall cutoffs of sedimentary horizons, entire displacement profiles have been measured for faults with a wide range of displacements (Cowie and Shipton, 1998; Maerten et al., 2001; Shipton and Cowie 2001; Shipton and Cowie, 2003). The Big Hole fault is located just to the South-East of the Chimney Rock Fault Array. While not explicitly part of the fault array, the Big Hole fault shares a nearly identical geological setting. The Big Hole fault has been extensively studied in detail as an analog to hydrocarbon reservoir-scale faults. Displacements on the exposed fault range from 8 m to 39 m. (Shipton and Cowie, 2001; Shipton and Cowie, 2003) Large networks of deformation band faults outcrop near Goblin Valley State Park on the southeastern margin of the San-Rafael Swell (Aydin and Johnson, 1978). Deformation bands are the result of concentrated shear deformation on narrow centimeter thick bands (Aydin and Johnson, 1978; Davatzes et al., 2003). Collapsing pore space accommodates this deformation. Deformation bands are interpreted as the embryonic stages of fault development (Fossen and Hesthammer, 1998; Fossen et al., 2007). Because deformation bands dramatically alter the local permeability structure, Goblin Valley has been extensively studied in light of fault nucleation and the implications for hydrocarbon circulation (e.g. Fossen et al., 2005; Tobari and Fossen 2009). At Goblin valley, arrays of deformation bands anastomose—outcropping as centimeter- to meter-sized slabs. These are often bounded by discrete slip surfaces with well-preserved striations — i.e. roughness (Aydin and Johnson, 1978). Offsets in sedimentary beds have allowed previous studies to obtain detailed displacement measurements (e.g. Schultz and Fossen 2002). Together, these field locations offer the chance to survey well-preserved fault surfaces that have hosted displacements from embryonic stages to 30 m of displacement. Moreover, novel to this study, we are able to survey multiple expressions of a single fault's surface with various displacements according the displacement profile of the fault.

Location	Lithology	Description	Displacement Constraints
Chimney Rock Fault Array	At the contact between the Navajo Sandstone and the base of the Carmel Unit	Orthorombic set of normal faults with preserved faults scarps of Navajo Sandstone	Displacement profiled of stratigraphic throw constrained by offset on a Carmel Limestone Marker Horizon by Maerten et al., 2000.
Big Hole Fault	Navajo Sandstone	One single large normal fault structure partitioning displacement on two major strands traceable for kilometers through a river wash with scarp exposure, and strike parallel/perpendicular cross-sectional exposure	Displacement constrained using the top Erosionally competent horizon at the top of the Navajo by Shipton and Cowie, 2003 and directly where possible.
Iron Wash	Navajo Sandstone	Network of normal and strike-slip cross-cutting faults. Little scarp exposure but has good cross-sectional exposure with fresh slip surfaces (using hammer and chisle)	Displacement mostly constrained by direct measurement of offset in the Upper Navajo horizon.
Molly's Castle	Entrada Sandstone	East-West striking network of normal faults and ubiquitous deformation bands. Well preserved slip surfaces broadly associated to a single slip surface structure intermittently bounding and crosscutting a thick (30 cm cluster of deformation bands	Displacement constraints available in places from mapping by Aydin (1978) and directly measured using various marker horizons within the Entrada Sandstone (e.g. laminae, cross-bedding unconformities, and thick red sandstone horizons depending on scale)

Table 1: Table caption

245 3 Field observations and Microstructure

246 The field observations and microstructures, in unison, build towards a qualitative characteri-
247 zation of fault maturation. I report on the fault architecture in the Navajo and Entrada Sand-
248 stones with a specific focus on the evolution from zero-displacement structures such as joints
249 and deformation bands to large offset structures with polished slip surfaces and accompanying
250 fault rock lithologies.

251 3.0.1 Fault architecture

252 Faults in the Navajo and Entrada sandstones generally record dip slip. Rotation of slip-direction
253 is typically associated points where larger fault structures crosscut each other. The general ar-
254 chitecture of the faults is complex. At all observable scales of observation, faults outcrop in
255 relays and cross-cutting conjugate sets typically dipping at 60° . The PSS fault model is only
256 rarely representative of the fault architecture. Fault zones rather have many slip surfaces,
257 sheared joints and splays which partition offset. As is characteristic for high porosity sand-
258 stone, fault zones all have deformation bands. The intensity of deformation bands decreases
259 exponentially away from the center of the fault zone and was shown to correlate in intensity
260 with displacement on the fault (cite someone). Deformation bands typically abut obliquely into
261 the slip surfaces at shallow angles (less than 70°). For an extensive review and description of
262 the faults in the Navajo and Entrada sand stones refer to Aydin's thesis.

263 1 or 2 : Photo j-i sketch of a cross-section through typical fault architectures

264 3.0.2 Zero-Displacement Structures

265 Deformations bands and joints are a ubiquitous and characteristic feature around faults in high
266 porosity sandstones. Larger fault structures nucleated from pre-existing networks of deforma-
267 tion bands and joints ([?]???). Deformation localizes and intensifies along theses structures to
268 then create through-going faults. The characteristics and surface morphology of these features
269 are especially relevant to our analysis as they represent the 'primordial roughness' of faults.

270 *Deformation bands* are recognizable in outcrop as sinuous white bands, 1 to 5 millimeters
271 in thickness, that accommodate shear offset. In sandstones, small strain can be mechanistically
272 accommodated by the run-away collapse of grains in sub planar sheets [?] ??. In thinsection,
273 ... The reduction of grain size and the associated compaction causes the deformation bands
274 to be stronger and more resistant to erosion than the host sandstone [?]. Unlike slip surfaces in
275 the area, deformation bands do not reduce the cohesion of the rock—they do not induce a well
276 define parting surface. Deformation bands preferentially resist erosion, often causing them to
277 protruded out of outcrops. *Deformation band clusters* accommodate more intense and localized
278 shear strain. The clusters are dense networks of anastamozing deformation bands ranging from
279 a few millimeters to tens of centimeters in thickness, often outcropping as slabs up to meters in
280 sizes (especially in the Entrada Sandstone). In the extensional regimes presented in this study,
281 clusters commonly form in upright conjugate pairs, each dipping 60° .

282 The edges of deformation band clusters that have eroded out appear to have a distinctly
283 corrugated and "lumpy" morphology (figure for this?). The orientation of the corrugations is
284 in clear agreement with cross-sutting slip surfaces kinematic indicators. The slabs are coated
285 with sand grains from the host sandstone. There is a clear directional asymmetry along the
286 direction of shear (see figure 1). Larger clusters often have one or many through going slip
287 surfaces. Cross cutting relationships along more mature fault structures show deformation
288 bands both pre-dating and postdating the nucleation of the fault. (*Probably need a figure for
289 this*). Please refer to Fossen, Shipton, Aydin for more detailed and extensive characterizations
290 of defomation bands in these localities.

291 Pre-existing regional joints sets are a common feature of every locality. Joints typically
292 have dips near 90° . Joints set are most readily measurable in the upper Navajo units and low
293 Carmel limestone pavements. The intensity of joint increases near the fault with the occurrence
294 of syn-kinematic sheared and splay joints. Refer to Aydin and Davatzes for extensive analysis
295 of joint characteristics and relative timing for each locality.

296 Systematic associations between the type and abundance of The Entrada unit is has more
297 deformation bands and fewer and less well defined joints. Moreover, in the Chimney Rock fault
298 array, there is a clear association to the conjugate fault set orientation. Faults striking



Figure 1: Left: Example of the edge of a deformation bands cluster at Molly's Castle. Note the "lumpy" morphology and an clear vertical directional asymmetry. Right: Cross-sectional view of a deformation band cluster with tens of centimeters of shear offset. It is unclear weather there is a through going slip surface localizing displacement. It is , however, definitely not on the edge of the cluster.

299 3.0.3 Slip Surfaces

300 Slip surfaces in the Navajo and Entrada sandstones are most readily identifiable by their vitreous
301 polish. Striations and grooves on the slip surfaces mark the direction of slip. In Cross-section,
302 slip surfaces are discrete, through-going and smooth relative to their zero-displacement coun-
303 terparts. Thin layers, less than a few centimeters in thickness, of milky white layers bound
304 typically bound the slip surface. The slip surfaces often cross-cut or bound deformation band
305 clusters. For a given slip surface, perpendicular profiles are notably more sinuous than slip
306 parallel profiles. Slip surfaces are only preserved in the Navajo and Entrada Sandstones. In
307 spite of good exposures in prospecting pits and careful inspection of the slip zone, the Navajo-
308 Carmel contact at the Chimney Rock fault array did not preserve good surfaces in the Carmel
309 Unit. It is unclear whether this indicates that the Carmel units is more susceptible to erosion
310 and/or alteration; or if a polished finish is only a feature of the quartzite sandstones. Pristine
311 fault slip surfaces are not cohesive, and always act as a parting surface. Fresh slip surfaces
312 uncovered *in situ* reveal a relatively consistent meso-structure (see figure – figure similar to
313 that in Jamies notes), A sharp interface, separated by a sub-mm thick layer of incohesive white
314 powder bounded by two vitreous surfaces is a dense set of deformation bands.

315 Surfaces that are notably more eroded and indurated have a reddish-brown to dark tarnish
316 and can loose their vitreous luster. Sections of the slip surface are plucked off. Severely
317 weathered scarps, not scanned in this study, develop a slip perpendicular fabric associated
318 to conjugate fractures and deformation bands abutting into the slip surfaces. Lichen grew
319 preferentially on north facing scarps. From our field observation, it is clear that erosion has
320 the effect of re-roughening the slip surfaces, especially at smaller scales. We can confidently
321 attribute these re-roughening effects to erosion because they did not occur in freshly parted
322 slip surfaces.



Figure 2: Left: Example of at least two distinct polished slip surfaces on the same fault structure. Right: Example of concentric pattern on cross-sectional view a fault

323 In thin section ...

324 The evolution of slip surfaces with displacement is qualitatively apparent

325 Faults with small displacements on the order of centimeters are distinctly different than
 326 larger displacement faults. They are visibly more sinuous, laterally discontinuous and less
 327 polished, instead, having a dull luster. They do not have well-defined gouge or cataclasites
 328 layers bounding the slip surface. In spite of extensive investigation, we do not observe faults
 329 with well-defined slip surfaces with clear offset markers indicating less than approximately half
 330 a centimeter of displacement.

331 Shipton showed clear instances of slip surfaces that had accommodated the overwhelming
 332 majority of fault offset. Displacement accommodated by smaller neighbouring discontinuous
 333 slip surfaces is minimal. More instances where larger displacement slip surfaces are unambigu-
 334 ously identifiable allowed us to characteristically further its characteristics generalized for the
 335 Navajo and Entrada Sanstones as follows:

336 • *Large displacement faults are distinctly more discrete and planar.*

337 • *Larger displacement faults are not cross-cut by deformation bands or more sinuous and
 338 discontinuous slip surfaces*

339 • *in line with the implicit definition of a fault, the PSS is nearly cohesionless.* Locations
 340 identified to be expose section of a PSS inevitably cracked open when sampling across the
 341 slip surface—the slip surfaces had no cohesion. Cohesion is typically thought to reinstate
 342 by precipitation and healing. We did not observe recovered healing in this study.

343 • *Large displacement faults have a vitreous finish;*

344 • *Large displacement slip surfaces are typically in the center of a damage zone.* Damage
 345 in an inevitable consequence of displacement and the accompanying mismatch that accu-
 346 cumulates. Damage at the field locations in this study is expressed as comminution (*e.g.*
 347 cataclasite and gouge), fragmentation (*e.g.* breccia, splay joints) and shear deformation
 348 (specifically deformation bands).

349 Microstructurally... (thin section + SEM pics)

350 3.0.4 Fault Rock

351 In this study, we refer to *fault rock* as rock altered either mechanically or chemically by the
 352 influence of the fault. The faults in our study area display a very diverse range in fault rock

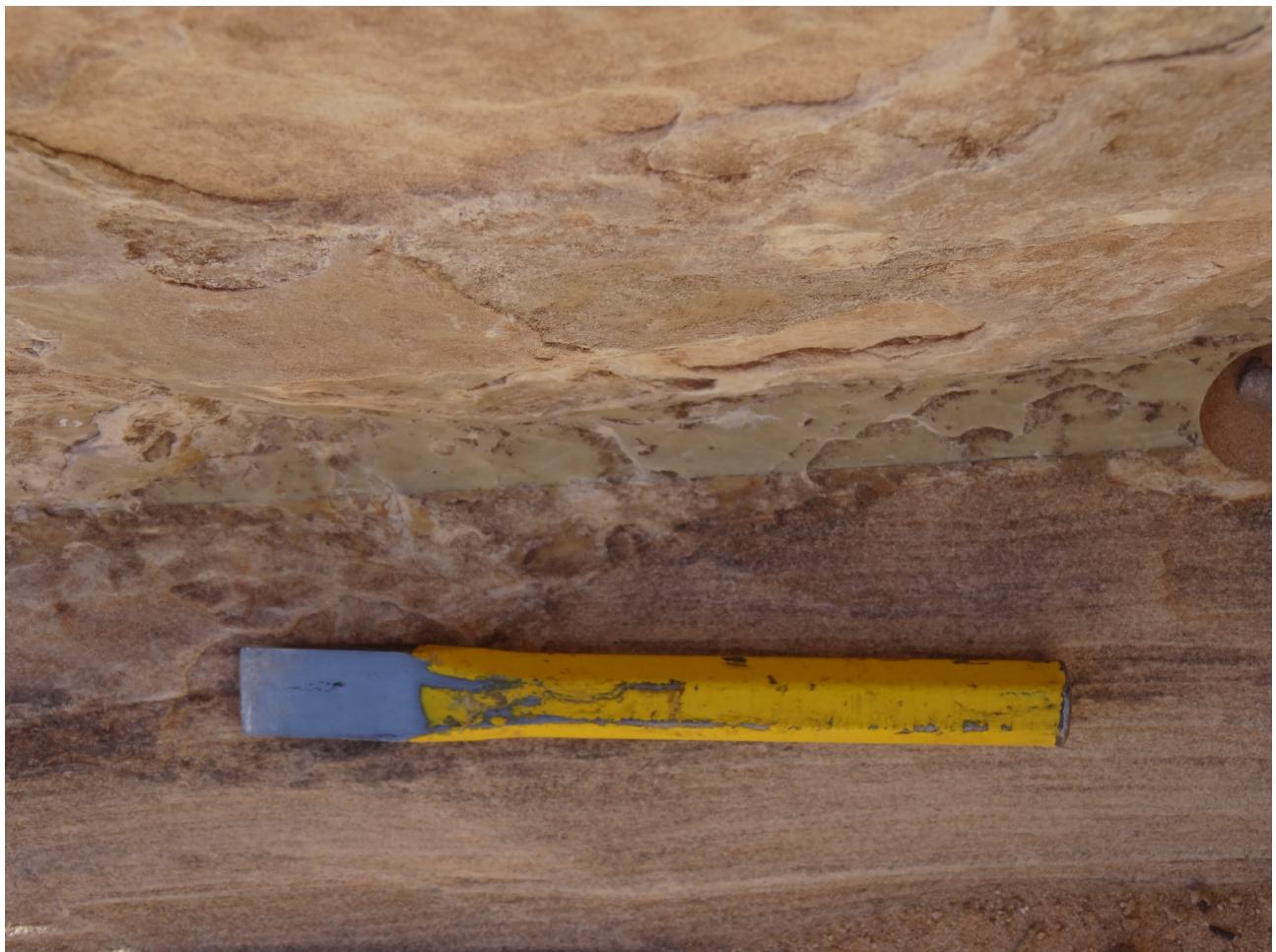


Figure 3: Example of a slip surface interpreted as a principle slip surface with around 20 meters of displacement at Big Hole Fault

353 lithologies, ranging from fine-grained cataclasites to massive bodies of breccias (up to meters of
354 thickness). Fault rock consistently bounds slip surfaces—often asymmetrically. However, both
355 the lithology and thickness of the fault rock are highly heterogeneous and are subject to drastic
356 changes at the outcrop scale (10's of meters) both along the strike and dip. We pay careful
357 attention to the fault rock as it is inevitably coupled to the slip surface roughness and its
358 maturation with cumulative displacement.

359 Healed Gouges - the spot at big hole - iron wash (powder between the surface) - micro-
360 structure - prospecting pit - typically on thinned sections of the fault rock (near the slip
361 surface) Cataclasites - big hole sample with slip surfaces on both sides of the cataclasite -
362 micro-structure - Breccias.... - thick sections of the Breccias occur lenses which range from cm's
363 to meters in thickness. Breccia clasts are typically poorly sorted and can be very coarse with
364 clast up to 10 cm in diameter. Clasts show indications for multiple generations of brecciation.

365 Thin Quarts lens - iron wash

366 Systematic associations between fault rock and fault structure exist. For instance, Davatzes
367 et al., 2002 reports of a systematic association between the fault rock lithology and the ori-
368 entation of the fault set. Namely, the orthorhombic fault set striking WNW has systematic
369 association with fragmentation—fault breccias; conversely the ENE fault set rather has slip sur-
370 faces cutting through deformation band clusters (see figure ??). This relation was speculated to
371 be the result of contrasting genetic mechanism. The WNW set is the result of the reactivation
372 of regional joints. In contrast the ENE fault set is the the result of clustering and anastamosing
373 deformation bands acting as a catalysing agent to the formation of a faults. In this study, we
374 observe clear instance of lithological contacts being associated to brecciation (photo at iron
375 wash where the top of the Navajo is brecciated and quickly reverts to a single fault strand.
376 More over, large breccia bodies are clearly related to points where faults are cross-cutting each
377 other at high obliquity as is often the case at the Chimney Rock fault array and

378 Complicating factors:

379 Associations between brecciation and lithological contacts...

380 Associations between brecciation and cross cutting faults...

381 3.1 Interpretation of field observations and roughness measurements

382 Cross-cutting relationships reported bot in this study and in previous work on faults in the
383 Navajo and Entrada units of the San-Rafael swell are particularly informative. Large dis-
384 placement slip surfaces are not cross cut by deformation bands and more sinuous slip surfaces.
385 However, large displacement slip surfaces do cross-cut clusters of deformation bands and more
386 sinuous slip surfaces. This relationship is indicative of a clear evolution of the fault architecture
387 by 1) localizing displacement and 2) smoothing out slip surfaces.

388 Faults zones with larger offset are associated to larger damage zones and more slip surfaces.
389 This is particularly telling fact when with the observation that small displacement slip surface
390 do not cross cut larger displacement slip surfaces.

391 The cross cutting relationship implies that either slip either smaller less continuous slip
392 surfaces predate the onset of the larger offset slip surface or that the they splay off of it.
393 However, we can reject the former as a possible mechanism as it does not account for the
394 increased density of slip surfaces on larger offset fault zones. This implies that they either form
395 directly from the stress heterogeneities induced by the roughness of larger displacement slip
396 surfaces.

397 Slip surfaces pre-dating large The former case stress heterogeneities from active slip surfaces
398 induced by fault roughness.

399 faults are smoother than joints or deformation bands

400 At the grains scale, grains are truncated, not ‘plucked’.

401 more linear fault traces where not offset by wavier fault traces

402 4 Quantitative analysis

403 4.1 Method

404 This study focuses on the qualitative and quantitative evolution of fault slip surfaces—both
405 addressing how fault slip surfaces evolve and the implications thereof. The quality of the
406 displacement measurements and the large number of accurate surface scans are fundamental
407 to the quantitative analysis of the data. Field-method and data acquisitions thus reflect these
408 standards.

409 For the qualitative analysis, we carefully record the characteristics of the fault architecture
410 in the context of fault evolution. Specifically, we are particularly meticulous about 1) identifying
411 cross-cutting relationships which indicate temporal evolution on the on fault, 2) identifying the
412 evolutionary stages in the formation of faults and 3) identifying and characterizing the wear
413 product, or fault rock, produce as faults evolve.

414 For the quantitative analysis, we collect scans both *in situ* and from hand samples collected
415 in the field. Scans are associated to a constraint on displacement. Moreover, for every scan,
416 the time of day, location, quality, strike and dip of the fault slip surface as well as the rake of
417 the slickenlines are recorded. When possible we record an estimate of the fault rock thickness.
418 Finally, we also record both a plan and cross-sectional view image of the scanned fault surfaces.
419 See appendix for the tabulation of this data. Together, all these measurements and observations
420 should provide the necessary data to robustly explain and quantify the process through which
421 faults mature.

422 4.1.1 Scan Data Acquisition

423 To measure slip surface roughness, we analyses large point clouds scans of real fault surfaces and
424 average the slip parallel and perpendicular spectral and statistical properties across hundreds
425 of profiles. Point clouds must be obtained across a flexible array of instruments to properly
426 capture the fractal scaling behavior (Brown and Scholtz, 1985; Candela et al., 2012). In this
427 study, we use three instruments with complimentary scales of observation. Together, these
428 instruments offer accurate and precise three-dimensional discretization of fault surfaces at over
429 nine decades of length scale.

430 *make a map of each areas with the location of every scan encoded with different symbols*

431 At the largest scales ranging from meters down to millimetres, a light detection and ranging
432 instrument (i.e. LiDAR). We use the LiDAR has been used in many previous studies of fault
433 roughness as it is easily deployable in the field and provides rapid means to collet very large point
434 cloud data set. However, its use is limiting as it requires exceptionally good and, accordingly,
435 rare exposure of fault surfaces that are large enough and fresh enough to not have been degraded
436 by erosion. In this study, we report 5 ??? Lidar Scans (see figure).

437 Instead, the bulk of *in situ* field measurements were made at intermediate scales ranging
438 from centimeters down to hundreds of microns with the NextEngine 3D laser scanner. The
439 NextEngine laser scanner is accurate down to 100 microns with resolution up to 41 540 points
440 per square centimeter. Note that the NextEngine is a much less cost prohibitive option when
441 compared to the LiDAR yet captures the same characters of the fault surfaces. The laser
442 scanner was benchmarked to a machined-flat granite surface and to a scan of the corona slip
443 surface both to industrial-grade laser scanner as reference. The scanner is not exactly built to
444 be field ready. It requires a power source, low light conditions, a stable surface to sit on, limited
445 dust exposure and must be connected to a computer. Moreover it only allows for a very limited

446 depth of field. To use the scanner in the field, we connected both the laser scanner and laptop
447 to a solar powered, *goal zero*, battery. The scanner was encased and padded in a reinforced
448 cardboard box with its depth exactly equivalent to the optimal depth of field. The set up had
449 the added advantage of being very portable, completely removing sunlight and limiting dust
450 exposure. We report XXX scans using the NextEngine Laser scanner.

451 Finally, hand samples were collected and analyzed with the Zygo blah blah, an optical
452 profilometer enabling accuracy from millimeters down to sub-micron. The Zygo blah blah
453 uses white light interferometry to produce relatively small point-clouds (XXX points) at various
454 magnifications. It does however allow for seamless stitching of scans. Individual and stitched
455 scans using the profilometer were benchmarked to a silicon carbide reference machined flat to
456 XXX meters. All samples were scanned at 20x magnification and stitched together to produce
457 sections roughly XXX by XXX millimeters. In addition, samples were scanned at the lowest
458 magnification to properly bridge the gap up to the laser scanner resolution. We report scans
459 of XXX samples with the white light profilometer, XXX of which were taken from surfaces
460 scanned in the field with the laser scanner.

461 4.1.2 Constraining displacement

462 We associate every scan with a displacement constraint. Field areas where specifically chosen
463 for the exceptional exposure and relatively simple offset markers. For the Chimney Rock Fault
464 Array and Big Hole Fault entire displacement profiles have been measured during previous
465 detailed mapping campaigns (i.e. Maarten shipton). At Iron wash, Horse Creek and Molly's
466 Castle, Atilla Aydin's mapping identified clear offset markers. Base maps for all these areas
467 were georeferenced onto satellite images and used in the field to streamline data acquisition.
468 Where fault exposure was good, we populated the maps with additional measurements using
469 basic tape measure and compass triangulation methods.

470 It is important to recognize that the base maps only report stratigraphic throw or, in some
471 cases, actual offset across *entire* fault zones. In the field we typically observe not one, but
472 many slip surfaces along with very complex networks of deformation bands and sheared joints
473 which partition displacement across many interfaces throughout the fault zone (see figure).
474 In this study, we make a distinction between *offset* across the entire fault and *displacement*
475 across a single fault slip surface. Without good marker horizons and cross-sectional exposure,
476 determining how stratigraphic offset is accommodated across slip surfaces can be ambiguous,
477 and thus requires detailed outcrop mapping (e.g. shipton ???) At Big Hole fault, two large-
478 scale continuous strands of the fault, both accommodating meters of displacement exemplify this
479 mechanism at a larger scale. In accordance, Shipton and Cowie, 2003 report large uncertainty on
480 the partitioning of stratigraphic offset across the two strands. This implies that offset across the
481 entire fault zone is an upper-bound constraint on displacement for a given slip surface. In XXX
482 of XXX fault slip surface measurements, this is the best available constraint on displacement.

483 We were able to reconstruct exact displacement and offset partitioning where cross-sectional
484 in the following specific cases: 1) If cross sectional exposure indicates that there is only a single
485 slip surface; 2) If cross-sectional exposure is good enough to clearly indicate the fault trace,
486 an offset marker (lamella, cross-bedding or lithological contact) and near enough to the slip
487 surface exposure; or 3) if it is unambiguous that one principle slip surface is accommodating
488 an overwhelming majority of displacement, i.e. it is continuous, it has a layer of fault rock and
489 it distinctly more linear and sharp than any other slip surface in the fault zone.

490 *make a table regarding the different types of displacement constraints*

491 known unknown equation assumptions N

492 - throw - assuming 60 deg dip, dip slip - throw, dip – assuming dip slip - throw, dip, rake –
493 assuming constant displacement orientation - direct off-set – with different permutations ...

494 4.1.3 Scan data Processing

495 I use point cloud spatial statistics to characterize and quantify active surface processes on faults.
496 I developed a *MatLab* work flow to entirely automate data processing from the raw *.xyz* input
497 format to the final statistical analysis:

498 1. Preprocessing

- 499 (a) manual inspection for coarsest defects
- 500 (b) Import *.xyz* data into *Matlab*
- 501 (c) Very coarse Height field filter
- 502 (d) Flatten points
- 503 (e) Grid data
- 504 (f) Orient grid along slip direction (using power spectral analysis)
- 505 (g) Remove defects
 - 506 i. Remove outliers in the height field
 - 507 ii. Fractal model filter
 - 508 iii. Remove abnormally flat (interpolated) sections

509 2. Processing

- 510 (a) Statistical analysis
 - 511 i. Scale dependent *RMS*
 - 512 ii. Scale dependent skewness
 - 513 iii. Scale dependent kurtosis
 - 514 iv. Scale dependent asymmetry
- 515 (b) Spectral Analysis
 - 516 i. Fast Fourier Transform (FFT)
 - 517 ii. Lomb-Scargle Periodogram

518 *make into figure, include bypasses and other recent additions*

519 Note that the general pre-processing workflow was slightly adapted according to the different
520 instruments that were used in the study. These adaptations were mostly attributable to the
521 quality of the data at the various scales of acquisition and the actual instrument specifications.
522 Scans collected with the LiDAR required more extensive manual point removal to avoid features
523 such as vegetation, spurious outliers and large defects to affect the quality of the preprocessing.
524 Scans collected at the intermediate scale with the laser scanner easily followed this workflow.
525 Finally, scans collected with the white light interferometer did require minimal preprocessing
526 and were aligned manually at the time of data collection.

527 Before conducting a statistical analysis scan data must be pre-processed into a workable
528 format. Scan data is a point cloud - a series of points with coordinates *x*, *y* and *z*. Scans reported
529 in this study typically have 10^6 to 10^7 points. In raw form, the point clouds are randomly
530 oriented, noisy and still contain instrumental and physical artefacts. Physical artefacts include
531 cracks, eroded sections, and vegetation; instrumental artefacts include noise, smoothing and
532 scattering. All these features must be removed. The process of manual removal is labour
533 intensive and unfeasible for a data set of the scope presented in this study. I rather opt
534 to automate this process. Only very large defects (defects that may substantially effect the
535 quality of finding a true mean plane) are manually removed.

536 The surface must first both be flattened and aligned along slip. Linear trends in the data
 537 induce an unwanted high frequency signal in data and also affect the quality of later interplo-
 538 lation onto a grid. Thus, x , y , z data is rotated using around the axis \mathbf{u} as determined by the
 539 normalized cross product between the surface normal \mathbf{n} and a vector normal to a flat surface
 540 ($\mathbf{n}_2 = [001]$):

$$\mathbf{u} = \mathbf{n} \times \mathbf{n}_2 / |\mathbf{n} \times \mathbf{n}_2|$$

541 with the rotation,

$$R = \cos \theta \mathbf{I} + \sin \theta [\mathbf{u}]_x + (1 - \cos \theta) \mathbf{u} \otimes \mathbf{u},$$

542 were $[\mathbf{u}]_x$ is the cross product matrix of u and \otimes is the tensor product and I is the identity
 543 matrix.

544 Fault surfaces are anisotropic. The direction of slip is preserved in the anisotropy whereby
 545 the 'smoothest' direction is slip parallel and the 'roughnest' direction is perpendicular to slip.
 546 The fault scan is rotated around the z axis such that the direction of slip is along the x axis.
 547 The direction of slip is by decimating raw data before iteratd steps of regridding, one-degree
 548 rotation and spectral analysis. In the radial search, roughness is quantified as the integral
 549 of the log-weighted power spectrum over the entire bandwidth of the sample surface. The
 550 angle associated to the minimum in roughness is then identified as the direction of slip and
 551 subsequently used to rotated the original flattened point cloud. The data is then interpolated
 552 onto a grid using a linear interpolation algorithm. The point spacing is automatically defined
 553 by the point density over the areal extent of the data:

$$\Delta x = N_{pts} / AXXXXXX \quad (6)$$

554 INCLUDE HISTOGRAMS FOR EACH FILTER

555 *Defects* include all physical surface features that are clearly not associated any faulting
 556 process, *e.g.* cracks, eroded patches, vegetation, etc.. Defects are idenetified and filtered out
 557 using combination of thresholding methods. These methods all revolve around identifying clear
 558 points or segments that are statistical outliers to the distribution characterizing the entire
 559 surface—abnormal points.

560 The most aggressive filter implemented searches for outliers to the fractal model. The filter
 561 removes entire linear segments with abnormally high variance in the height field for the given
 562 scale of observation. For this implementation, I iterate over 10 filter scales. The scales are
 563 selected using a log spacing from the 10 points up to the length of the entire surface. The
 564 threshold for segment removal is chosen to be four standard deviations from the mean (should
 565 account for < 0.1 percent of the data in a normal distribution). Note that, assuming a normal
 566 distribution of variance data for a given scale, the filter should not induce a systematic bias since
 567 the filtering is symmetric around the mean. However, surface features associated with a truly
 568 distinct mechanism of formation, in this case cracks and other defects that will typically have
 569 much higher variance, *are* be removed. This general approach ensures that defects, regardless
 570 of their scale get identified and removed. This is important for any subsequent fractal analysis.

571 Abnormally flat sections arise as the result of triangular interpolation of sparse points.
 572 Typically, interpolation on the edge on a non-convex set of points is subject to this effect.
 573 These artefacts are readily identified in the curvature data. In the log-transformed absolute
 574 value curvature field, these sections appear to be nearly or exactly zero. The filter rejects
 575 point with curvatures less than 10^{-25} . These values likely associated to the linear interpolation
 576 scheme.

577 Finally, all scan are inspected to make sure that the pre-processing was successful. The
 578 script fails to properly process scans that are excessively populated with surface defects. These

579 scans were manually cleaned and oriented before re-processing them. Manual changes were
580 executed in *CloudCompare*.

581 Pre-processed scans are N by M scalar fields of fault surface topography (the sitance from
582 the mean plane) aligned with slip along the x axis. NaN values mark locations where data is
583 missing or was removed by filters. Point spacing is defined the mean point density of the scan
584 in the x - y plane.

585 4.1.4 Statistical Analysis

586 After pre-processing, scans discretize defect-free slip surfaces with grids with rows aligned
587 with the slip direction. We compute the power spectral density content for every continuous
588 segment of every single profile of the grid using a Fast Fourier Transform (FFT). Individual
589 spectra are interpolated onto a master frequency vector. For a given frequency, the distribution
590 of power values across the profiles through along the slip is strongly skewed (see figure xxx).
591 The skewness is attributable to the non-negative constraint on power and residual outlying
592 profiles (defects not properly removed). To provide a more representative and robust measure
593 of maximum likelihood, we use the geometrical mean instead of the arithmetical mean. Ac-
594 cordingly, errors represent the 1σ range in the log-transformed distribution. The analysis yields
595 one representative spectrum for each scan.

596 The spatial frequency content of slip surfaces follow a power law. This characteristic is
597 roughly fixed for a single slip surface regardless of the scale sampled in our instrumental array.
598 Fixed scaling and its power law form in frequency space is a feature of the fractal character of
599 fault surfaces. We can thus further distil the roughness measurements using the fractal model
600 of the fault:

$$P(k) = Ck^{-\beta} \quad (7)$$

601 Accordingly the entire spectral information of a scan can be summarized with the prefactor
602 (C) and the scaling exponent (β). Determining fractal parameters from spectra is not trivial.
603 *A priori*, the fractal model is determined using a weighted power law regression through the
604 spectra. Weights are determined according to the inverse $1\sigma^2$ variance of the power estimates.
605 However, confidence interval on the fit parameters are strongly sensitive to both instrumental
606 and analytical biases (XXX schittbulh 1998). Biases induce unwanted high or low pass filters
607 in the spectral content-amplifying or diminishing selective bandwidth. The combination of
608 instruments and highly overlapping bandwidths provides a means to identify the affected sec-
609 tions and suppress methodological bias. The comparison of the power law fit through multiple
610 heavily overlapping instrumental bandwidths to the representative spectral of individual scans
611 highlights instrument-specific biases. In doing so, we identify conservative bounds on sections
612 of frequency spectrum that deviated from the power law fit. For our instruments, we find that
613 artefacts are particularly disruptive at the small scale instrumental limit. The LiDar and laser
614 scanner are dominated by a shallower slope at the high frequency tail of the spectra which
615 has been interpreted in previous studies as random noise (XXX). Conversely, the spectra of
616 the scan collected using the white light interferometer have steeper high frequency tails. This
617 artefact has not been reported in previous studies in spite of the extensive use of the instru-
618 ment. This discrepancy is likely attributable to the comparatively limited and subdued use of
619 aggressive smoothing filters both in the scan data and in the spectra our analysis. Affected
620 bandwidths are omitted from subsequent analysis. In spite of this approach, small discrepan-
621 cies in parametrization of the power law fit for a given slip surface render the extrapolation of
622 measurements from on instrumental bandwidth to the other instrumental scale of limited use.
623 We therefore choose to report any further results at the bandwidth or specific wavelength best
624 captured by the instrumental magnification.

625 INCLUDE A FIGURE WITH: ORIGINAL SURFACE, AUTOMATICALLY PROCESSED
 626 GRID, MANUALLY PROCESSED GRID AND CORRESPONDING POWER SPECTRA.
 627 identifying fractal scaling section plot of white light all magnifications computational scheme
 628 to select the good section error on direct displacement estimates?

629 4.2 Results

630 4.2.1 Roughness measurements

631 figures to include:

- 632 • all spectra
- 633 • increasing anisotropy (two surfaces) - polar plot

634 Figure XXX shows the all the PSD calculations obtained from the scans collected in this
 635 study. Consistent with previous work, we find that the PSD spectra over the entire bandwidth
 636 reported in this study generally follow a power law scaling (a linear relation in log-log space).
 637 This feature corresponds to the constant fractal scaling. The scaling exponent and pre-factors
 638 are calculated using linear least-squares fit of the spectra in log-log space. The Hurst exponent
 639 can then be obtained according to equation XXX.

640 In the slip perpendicular direction, Hurst exponents range from XXX to XXX, with an
 641 average value of 0.8ish; Prefactors range from XXX to XXX with an average value of XXX. In
 642 the slip parallel direction, Hurst exponents range from XXX to XXX, with an average value
 643 of 0.8ish; Prefactors range from XXX to XXX with an average value of XXX. Implicit to the
 644 pre-processing grid alignment, for any single scan the slip parallel direction is systematically
 645 smoother than the slip perpendicular direction indicating a clear surface anisotropy. The entire
 646 data set does however indicate an overlapping range in slip parallel and perpendicular directions.
 647 We also note that lower pre-factors are generally associated to lower Hurst exponents.

648 An evolution with displacement is weakly expressed in the spectral analysis but is cluttered
 649 and obscured by highly variable errors on displacements and roughness measurements. In
 650 order to highlight the effect of displacement on the surface roughness, we separate our scan
 651 data into two distinct populations. 1) Scan data with direct displacement constraint and
 652 2) scan data associated to maximum displacement constrains. Brodsky et al., 2011, tested
 653 the validity of a power law relation between fault roughness at various specific scales and
 654 displacement. Building upon this approach, we use both data populations to test the validity
 655 and parameterization of the fit and the Implicit hypothesis that faults smooth as a function of
 656 displacement—the smoothing model. Scan data with direct displacement constraints serves as a
 657 direct test and a means to parametrize the smoothing model. For the model to be valid it must
 658 agree with further constraints imposed by data with only maximum displacement estimates.

659 A point defined by the maximum error bound on displacement and the roughness of the
 660 fault surface is in agreement with smoothing model if it is rougher than roughness prescribed
 661 by the model as parametrized by direct measurement. Conversely, if the point is rougher than
 662 the model prediction, it is not physically possible in the model construct. A null hypothesis
 663 would prescribe no bound on the roughness and would simply have the predicted roughness
 664 of a fault be defined by the probability distribution function of the entire roughness dataset.
 665 Accordingly, we can roughly estimate the probability that our distribution of data relative to
 666 the smoothing model is a random element of chance according to:

$$P = \prod p(y_i > Y(x_i)) \quad (8)$$

667 Figures XXX to XXX shows the relation between roughness and displacement as interpo-
 668 lated a various scales of observation. Vertical error bars on the power spectral density are

669 obtained from the confidence interval of the of the fractal model regression. Horizontal error-
670 bars on displacement are defined on a case by case basis from field observations and previous
671 work in on the fault arrays. We present both the fit through the our entire dataset (comprised of
672 direct and upper bound constraints on displacement) and through the the directly constrained
673 displacement estimates. Fits are obtained using a least squares linear regression through the
674 log-transformed data sets. In order to provide error bounds on the fit parameters, we use a
675 full Monte Carlo simulation sampling direct displacement estimated as Gaussian distributions,
676 upper bound displacement constrains as completely random distributions across the entire pos-
677 sible range of displacements and power spectral density estimates as log normal distributions.
678 Errors represent on standard deviation estimated from 10000 simulations.

679 The weak trend across the entire dataset imply and expectation of smoother slip surfaces
680 in fault zones which have accommodated larger displacement.

681 Conversely the stronger trend across the well constrained data implies that an individual slip
682 surface smooths with displacement. The smoothing exponent varies according to the different
683 scales of observation (XXX at the laser at the centimeter scale, XXX at the millimeter scale
684 and XXX at the micron scale). While a power law fit to the best constrained measurements
685 is has poor fit metrics, we find a nearly perfect agreement with roughness measurements only
686 associated to upper bound constraints.

687 Two constraints on displacement – two data populations plot of all the spectra color coded
688 with displacement smoothing plots: parallel - ζ all scales perpendicular - ζ all scales Hurst expo-
689 nent - ζ all scales Fit for smoothing through direct data, discuss consistency with max disp data
690 Other statistical metrics? Poly-gaussian features in the surface roughness Skewness of height
691 field as a function of scale Null result worth reporting? Do a plot of the evolution of skewness
692 at the grain scale?

693 qualitative illustration of maturity

694 4.3 Hard facts

695 The following is a list of ‘hard facts’ that can be established from the both the qualitative and
696 quantitative data:

- 697 • faults are smoother than joints or deformation bands
 - 698 – power spectrum shows that fault slip surfaces are systematically smoother than joint
699 and deformation band surfaces at all wave lengths reported in this study (10^{-6} to
700 10^5 meters)
- 701 • At the grains scale, grains are truncated, not ‘plucked’.
- 702 • The roughness of a slip surface is sensitive to its displacement history. This result is robust
703 across multiple faults both nucleated from deformation bands and joints and variations
704 in fault rock and host rock lithology.
- 705 • The smoothing exponent is likely more than 1 at certain scales - quote from Emily: “In
706 all of these cases, the scatter of the data is large, but the basic result holds: the absolute
707 value of the exponent is much less than 1.”
- 708 • The smoothing rate is highest at small displacements and decreases with displacement.
- 709 • Smoothing occurs at all scales of this study
- 710 • a slip surface from a large offset fault is more likely to be smoother

- 711 • for any given the displacement on a fault, the smoothest slip surface roughly follows the
 712 same smoothing trend as that defined by direct displacement measurements.
- 713 • The roughness varies spatially on a slip surface - the scatter in the data exceeds the
 714 instrumental error
- 715 • the height distribution of points on a slip surface can be far from normally distributed.
- 716 • the Hurst exponent has a very large range in values (less than Zero to 0.9)
- 717 • more linear fault traces where not offset by wavier fault traces

718 5 Model

719 5.1 Modelling Objectives

720 5.2 Model Outline

721 In this study, we utilize work minimization numerical modelling to capture the growth of fault
 722 damage and the effect of rough asperities. The models are built off of fric2d and growth by
 723 optimization of work (GROW) developed by Michele Cooke and Jessica McBeck.

724 5.2.1 GROW

725 Growth by optimization of work predicts fracture propagation paths. It does so by minimizing
 726 the external work on the system. The model theoretically allows for the simultaneous growth
 727 of multiple fractures and

728 The general algorithm uses a boundary element method to describe the fractures-linear
 729 dislocation elements that discretize the entire length of the fault. As a crack grows, dislocation
 730 elements are added radially to the tip of the crack so as to minimize the external work on the
 731 system normalized by the crack area ($W_{ext}/\Delta A$). External work is further defined as:

$$732 W_{ext} = \oint (\tau u_s + \sigma_n u_n) dB \quad (9)$$

733 5.3 Model Results

734 6 Discussion

735 6.0.1 Tying the model together with roughness measurements and model

736 wear rate (character), tying together model with

737 6.1 An external estimate of gouge production and fault thickness

738 The data collected in this study offers the unique opportunity to provide new indirect estimates
 739 of fault rock production, fault thickness and dilation rate over an entire fault. We know that
 740 1) the primordial roughness is systematically rougher than mature faults, 2) the primordial
 741 roughness is relatively constant, and 3) the roughness can be estimated for a given displacement.
 742 Using these results, I will estimate the volume of fault rock produced through wear and the
 743 corresponding roughness induced accommodation space in the fault system.

744 Displacing two rough fractal surfaces in shear requires dilation. The expectation dilation
 745 can be estimated according to the amplitude of the largest wavelength (λ) being offset (see

745 figure XXX). For a given displacement, u , the largest wavelength in the system will be $\lambda = 2u_i$.
 746 Using a fractal paradigm to define the average amplitude of a given wavelength according to
 747 the pre-factor β and the Hurst scaling exponent, H , (*reference the equation*) we find that
 748 the dilation, A can be expressed as a function of displacement:

$$A(u) = \sqrt{\beta 2u^{-2H-1}} \quad (10)$$

749 If we apply this to an entire fault system with displacement field, U , we can estimate the
 750 void space that would be produced:

$$V_{void}(U) = \int_S \sqrt{\beta 2U^{-2H-1}} dS \quad (11)$$

751 Since the fault system is closed any change in fault roughness *must* be coupled to the fault
 752 core. If all changes in the fault surface are associated to a production of fault rock, we can
 753 effectively estimate the volume of fault rock that has been produced from displacement u_0 to u_f
 754 by comparing the volume integral under the corresponding initial and final slip surfaces $S(u_0)$
 755 and $S(u_f)$.

$$\frac{\Delta V_{faultrock}}{\Delta u} = \int_S S(u_0) - S(u_f) dS \quad (12)$$

756 volume integral under the surfaces, S , can be estimated numerically according to the fre-
 757 quency distribution prescribed by the RMS the entire fault system. Note that the RMS is
 758 estimated at the length scale of the entire fault; wear processes are active at all length scales
 759 below this.

$$\int S dS \approx \quad (13)$$

760 Now for the displacement field, U , we can estimate the total fault rock produced by using
 761 the primordial surface roughness, $S(0)$, and the prediction of the surface roughness extrapolated
 762 to the length of the fault (* reference the the equation of smoothing *) such that:

$$V_{faultrock}(U) = \int_S S(0) - S(U) dS \quad (14)$$

763 The comparison between the two quatities is telling. If the amount of fault rock is

7 conclusion

7.1 future work

8 Appendix

8.1 Surface Processing scripts

768 Or possibly a link to a git repository...

8.2 User manual for script

770 This manual should serve as both a basic guide to the logic and usage of the *surface processing*
 771 *package*.

772 The master function of the package is *surfaceprocessing*. This function effectively deal with
 773 the inputs and direct computations towards the necessary functions. Outputs of the function

774 are a .mat workspace file for each input data file. The workspace includes a structure (called
775 *parameters*) with the raw surface analysis outputs, the point spacing, the decimation factor (if
776 any), the file name and the date of the analysis. The workspace also includes the grid form of
777 the original inputted surface (called *surface*), and the pre-processed copy that was used for the
778 subsequent analysis (called *zGrid*). Inputs are always included in pairs. The former defines the
779 type of input, the latter qualifies or quantifies the input. This structure allows for adaptability
780 of the code to various needs. Options include the following:

- 781 • *what to do?*: 'ToDo', followed by the desired analyses on of: 'FFT', 'PLOMB', 'parameters'
782 or 'all' (default is 'all') - can be a cell array. This specifies what kind of spatial analysis
783 will be done on the input surface data. The spatial analysis is calculated and averaged
784 across every single profiles along the surface. The analyses are the following:

- 785 – 'FFT', a power spectrum computed using a Fast Fourier Transform (FFT) algorithm;
- 786 – 'PLOMB', a power spectrum computed using a least-squares Lomb-Scargle algo-
787 rithm;
- 788 – 'paramters', the calculation (as a function of scale) of the Root Mean Squared (RMS),
789 skewness, kurtosis and asymmetry averaged across all segments of a given length on
790 all profiles of the surface.

791 'all' simply performs all the analyses outlined above.

- 792 • *skip pre-processing?*: 'bypass', followed by 'zygo', 'pre-processing' or 'no' to be used
793 input is already in aligned clean grid form - input files are then (default is 'no'). 'zygo'
794 is specifically adapted to the proprietary data format of the white light in Wong. 'pre-
795 processing' simply skips any pre-processing. This option requires a .mat structure with
796 a field named 'grid' with the topography and a field name 'pointSpacing' specifying the
797 point spacing (in meters). In either case the topography must be aligned such that the
798 positive x direction is the parallel direction.
- 799 • *for the parameter analysis, how many scales?* 'numberOfScales' followed by the desired
800 number of analysed scales. This option is relevant to the parameters analysis. Note that
801 this has a lot of effect on the amount of processing time (default is 10).
- 802 • *decimation*: 'decimationFactor' followed by the desired decimation factor (default is 1).
803 Decimation is a useful tool to reduce computation time. The surface grid is sub-sampled
804 according to the decimation such that a decimation factor of k would imply that only
805 every k th point on the every k th will be considered for hte subsequent analysis.
- 806 • *Instrument specific analysis* 'instrument' followed by 'white light', 'laser scanner' or 'lidar'
807 (default does not set any instrument specific adjustments). Some instrument specific pre-
808 processing steps are taken. Please contact me if you intend to use this as they may be
809 highly dependent on the specific instrument used.

810 For instance, *surfaceprocessing('todo','FFT','bypass','zygo')* will only perform a power spec-
811 tral density analysis and will skip preprocessing and assume that all input will be in the 'zygo'
812 export .xyz format.

813 When the command is executed, the user will be prompted to navigate to the directory
814 where the input data is located. IMPORTANT: the directory must *only* contain files of one
815 data format. There cannot be other files or sub-directories in the directory. The user will then
816 be prompted to choose a destination for the output data. The requirements for the output

817 location are less stringent. However, it is advisable to choose an empty directory such as to
818 facilitate subsequent steps.

819 The next step is to visualize the output of the analysis. This is done using the *unpack*
820 *parameters* function. This function provides various visualization options for all files in the
821 directory chosen by the user. The first input (the *desired plot*) can be one of the following:

822 'FFT': plot all power spectra;
823 'PLOMB': periodogram plot as determined by the Lomb-Scargle least squares analysis;
824 'topostd': plot of the root mean squared (RMS) as a function of scale;
825 'topoSkew': plot of skewness of height fields as a function of segment scale;
826 'topoKurt': plot of the kurtoisis of height fields as a function of segment scale;
827 'PowerVsDisp': plot of power interpolated at a given scale as a function of displacement;
828 'RMSVsDisp': model RMS at a given scale as a function of displacement
829 'Grids': shows both the original and pre-processed grid for the specified file 'fileName';
830 'Best Fits': best logarithmic fits to power spectra obtained from the fast fourrier trans-
831 form analysis.

832 The functionality of the packages is broadly divided into three sections: 1) importing and
833 preprocessing data, 2) performing various spatial statistics on the pre-processed data, and 3)
834 unpacking the analysis output into figures.

835 In order to run smoothly the all functions included in the package should be kept in the
836 same directory or on an accessible path.

837 For reference, here is a quick outline of what each function does:

838 `affine fit`: (from mathworks) Computes the plane of best fit using least squares normal
839 distance;
840 `align grid`: finds the smoothest directions in a grid using FFT spectra and rotates and
841 re-grids the input grid;
842 `fault spectral density simple`: Calculates the average lomb-scargle spectral density every
843 row of a N by M array;
844 `FindErr loop anisotropy`
845 `flatten XYZ`: removes planar trends from XYZ data by applying a rotations matrix ac-
846 cording to the best fit plane (`affine fit`);
847 `fractal model outlier`: Removes outlying segments according to a near-gaussian model for
848 the distribution of RMS values at specified segment lengths (or scales);
849 `frequency spectrum`: Calculates the average lomb-scargle spectral density of all continuous
850 segments on every single row of a N by M array;
851 `parse zygo format`: extracts the both the point spacing and topographic grid from the
852 exported zygo format. Can also remove planar trend from data (substracted from grid);
853 `rotateZ`: applies rotation matrix on XYZ data

854 *surface`analysis*: Aggregates the analysis functions and applies them to an input grid
855 *surface`cleaning*: removes outliers associated to surface defects
856 *surface`parameters*: calculates spatial statistics and parameters along segments as a func-
857 tion of scale (RMS, skewness, directional asymmetry and kurtosis)
858 *surface`preprocessing`2*: deals with preprocessing input data (import data, cleaning and
859 gridding data)